Magnetically Modulated Pot-Like $MnFe_2O_4$ Micromotors: Nanoparticle Assembly Fabrication and their Capability for Direct Oil Removal

*Fangzhi Mou, Deng Pan, Chuanrui Chen, Yirong Gao, Leilei Xu, and Jianguo Guan**

J.G.G. dedicates this work to his loved mother, who passed away on April 3, 2015

This work demonstrates a simple-structured, low-cost magnetically modulated micromotor of $MnFe_2O_4$ pot-like hollow microparticles as well as its facile, versatile, and large-scale growing-bubble-templated nanoparticle (NP) assembly fabrication approach. In this approach, the hydrophobic $MnFe_2O_4$@oleic acid NPs in an oil droplet of chloroform and hexane assembled into a dense NP shell layer due to the hydrophobic interactions between the NP surfaces. With the encapsulated oil continuously vaporizing into high-pressured gas bubbles, the dense $MnFe_2O_4$ NP shell layer then bursts, forming an asymmetric pot-like $MnFe_2O_4$ micromotor by creating a single hole in it. For the as-developed simple pot-like $MnFe_2O_4$ micromotor, the catalytically generated O_2 molecules nucleate and grow into bubbles preferentially on the inner concave surface rather than on the outer convex surface, resulting in continuous ejection of O_2 bubbles from the open hole to propel it. Dexterously integrating the high catalytic activity for H_2O_2 decomposition to produce O_2 bubbles, excellent magnetic property with the instinctive surface hydrophobicity, the $MnFe_2O_4$ pot-like micromotor not only can autonomously move in water media with both velocity and direction modulated by external magnetic field but also can directly serve for environmental oil removal without any further surface modification. The results here may inspire novel practical micromotors.

1. Introduction

Self-propelled micro-/nanomotors are capable of converting chemical energy into autonomous motion generally due to the asymmetry in chemical compositions and/or morphologies.[1] They may demonstrate fascinating capabilities to pick up, transport, and release various micro-/nanocargoes in liquid media, and thus have important potential applications in drug delivery, protein and cell separation, microsurgeries, and environmental remediation, etc.[1,2] According to the attribution of the driving forces exerted on the micro-/nanomotors, two typical propulsion mechanisms of the phoresis and bubbles have been proposed, where the propulsions are originated from the concentration gradients of resultants and the recoil force of bubble ejection, respectively. Compared to the phoresis-propelled micro-/nanomotors, those propelled by bubbles could show some impressive features including a strong thrust, ultrafast movement speeds, and independence of motion on ionic strength in liquid media.[3] Particularly, the bubble-propelled catalytic micromotors (BCMs) show the additional advantage of a long life span and have thus received much attention in the last decade.[4]

To achieve the practical application of the BCMs, they should be steered in a predesigned way, involving controllable motion state, moving speed, and trajectory, etc.[2e,5] On the basis of this clue, various strategies of external stimuli have been recently developed in an attempt to control the motion of the BCMs, including external light, ultrasound, thermal and magnetic field, etc.[6] Among them, the magnetic field could operate magnetic BCMs with a high spatial and temporal resolution.[5] For example, they may repetitively "stop-and-go" or "stop-turn-and-go" under a tunable magnetic field. However, the so far developed magnetic BCMs are generally designed with a complex multilayered tubular or Janus colloid structure.[6c,7] They can be obtained only when a magnetic component is inserted between a catalyst layer (Pt, Ag, or catalase) and an inert layer (polymer or Ti) by complex and expensive processing techniques, including the "rolled-up," vapor deposition, and template-assisted electrodeposition methods.[4a,8] Consequently, their production is only restricted to the laboratories equipped with advanced fabrication facilities and this greatly hinders their practical use. Therefore, there are urgent demands for the creation of new design strategies to simplify the structures of magnetic BCMs as well as the development of their facile, large-scale fabrication approaches.

In this work, we have developed a novel magnetically modulated micromotor of single-layered $MnFe_2O_4$ pot-like hollow microparticles with a capability to directly remove contaminant

Dr. F. Z. Mou, D. Pan, C. R. Chen, Y. R. Gao, Dr. L. L. Xu, Prof. J. G. Guan
State Key Laboratory of Advanced Technology for Materials Synthesis and Processing
Wuhan University of Technology
122 Luoshi Road, Wuhan 430070, P. R. China
E-mail: guanjg@whut.edu.cn

DOI: 10.1002/adfm.201502835

oils from water. The formation mechanism of the asymmetric pot-like $MnFe_2O_4$ micromotors is proposed to be a growing-bubble-templated nanoparticle (NP) assembly. For such a simple pot-like $MnFe_2O_4$ micromotor in H_2O_2 aqueous solution, the catalytically generated O_2 molecules will nucleate and grow into bubbles preferentially on the inner concave surface rather than on the outer surface, leading to a vital propulsion of the micromotor. Attributing to the fine magnetic responses, the motion of the micromotor can further be adjusted wirelessly by a modulated magnetic field. Compared to the reported micromotors for environmental oil remediation, which have a complex multilayered structure and need an additional surface modification with long-chain alkanethiols,[9] the as-developed $MnFe_2O_4$ micromotors have a simple single-layered structure and can be directly used for environmental oil remediation without any further surface modification because of the hydrophobic surface endowed by the pre-existed oleic acid long chains. The as-proposed formation mechanism can be applied to construct other metal oxide pot-like nanostructures (such as TiO_2 pot-like nanostructures) used for microreactors, energy storage, and conversion, as well as environment remediation.[10] The micromotors developed here may inspire novel design strategies for the practical micromotors due to the low cost, simple structure as well as the facile, large-scale fabrication approach.

2. Results and Discussion

Our designed simple-structured magnetic micromotors are single-layered $MnFe_2O_4$ pot-like hollow microparticles. They can be easily fabricated in a large scale by moderately warming volatile oil droplets consisting of hydrophobic $MnFe_2O_4$@OA NPs (Figure S1, Supporting Information) in an aqueous solution. **Figure 1**A shows that the as-fabricated $MnFe_2O_4$ micromotors have a typical pot-like structure with a hollow interior and a single open hole in the shell. The average diameter (d) of the micromotors is about 25 μm, and the open holes on its surfaces have a diameter of about 10 μm. Close observation of a typical broken pot-like microparticle (Figure 1B) reveals that the hollow interior is biased to one side of the microparticle. Both the inner and outer surfaces are smooth, and the wall thicknesses near and away from the open hole are about 500 nm and 4 μm, respectively. The X-ray diffraction (XRD) pattern in Figure 1C can be indexed to cubic $MnFe_2O_4$ (JCPDS 73–1964).[11] The obvious broadening diffraction peaks indicate that the pot-like $MnFe_2O_4$ micromotors are composed of nanocrystals, whose size can be estimated from the full width at half maximum to be about 6 nm according to the Scherrer's formula. The thermogravimetry (TG) and differential scanning calorimetry (DSC) analyses (Figure 1D) reveal that the as-obtained pot-like micromotors contain 86.1 wt% $MnFe_2O_4$.

To decipher the formation mechanism of the as-obtained pot-like $MnFe_2O_4$ micromotors, we have investigated in detail the time-dependent structural transformation process by an optical microscope. After a mixed volatile oil of chloroform and *n*-hexane (8.8:1.2 in volume) containing $MnFe_2O_4$@OA NPs was added into the aqueous solution with 3.0×10^{-3} M cetyltrimethylammonium bromide (CTAB) and magnetically stirred for 60 s, a suspension of tiny oil droplets containing $MnFe_2O_4$@OA NPs in an aqueous solution with CTAB was formed. Video 1 (Supporting Information) and **Figure 2**A show that when the suspension is heated at 37 °C, the oil droplets

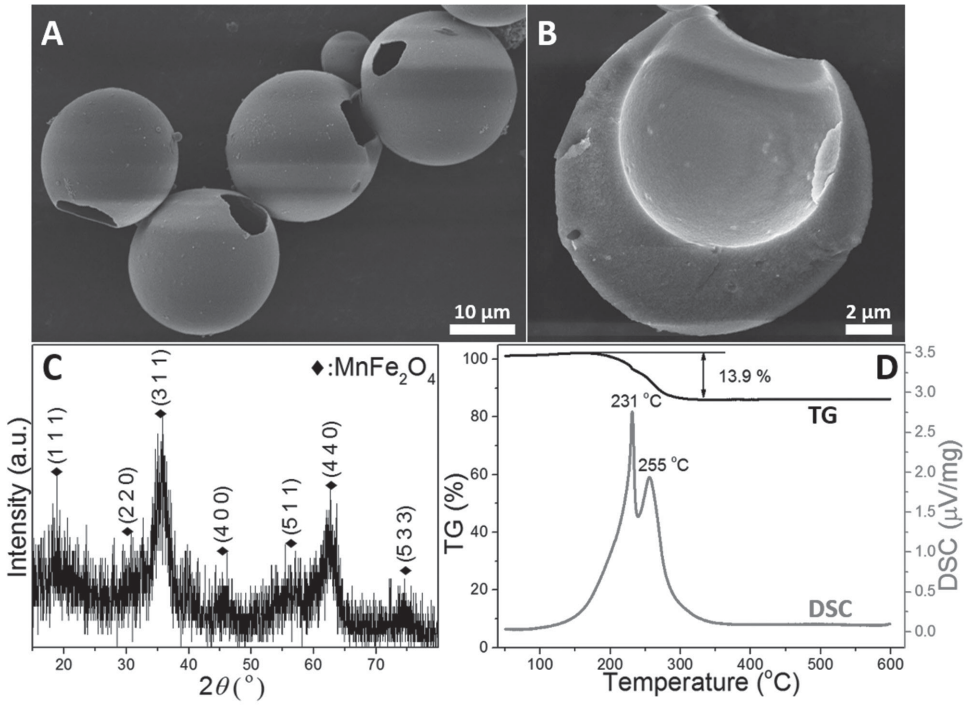

Figure 1. A,B) SEM images, C) XRD pattern, and D) TG–DSC analysis of the as-assembled $MnFe_2O_4$ micromotors. Panel (B) represents a typical cross-section morphology of the as-assembled $MnFe_2O_4$ micromotors.

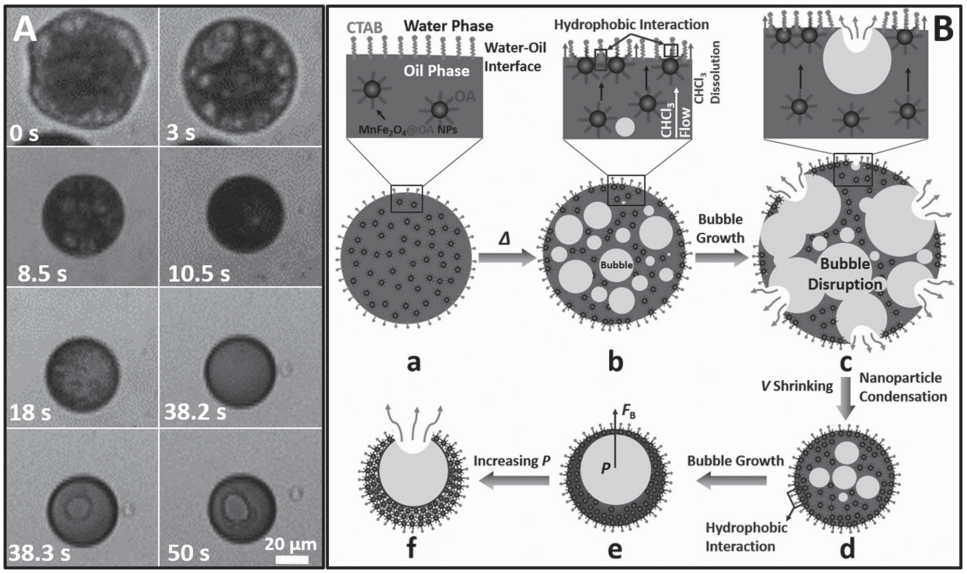

Figure 2. A) Optical images taken from Video 1 of the Supporting Information, which shows the transformation from an oil droplet of mixed volatile chloroform and *n*-hexane (8.8:1.2 in volume) containing $MnFe_2O_4$@OA NPs suspended in an aqueous solution with 3.0×10^{-3} M CTAB at 37 °C into a pot-like $MnFe_2O_4$ micromotor by prolonging the heating time; B) schematic illustration for the formation mechanism of the pot-like $MnFe_2O_4$ micromotors by the growing-bubble-templated self-assembly of hydrophobic $MnFe_2O_4$@OA NPs in a volatile oil droplet: a) The oil droplet containing $MnFe_2O_4$@OA NPs in the bulk water phase would experience intensive evaporation of volatile oil phase during the heating process. b,c) The $MnFe_2O_4$@OA NPs are carried to the oil–water interface and assembled there due to the outward diffusion flow of chloroform. d) When most of the solvents inside the oil droplet are evaporated, the NPs are assembled into a dense shell, which could trap gas bubbles generated by the inside evaporated oils. e) Further evaporating oils enable the encapsulated bubbles to merge into one big bubble, which is biased toward the upper side of the oil droplet under the action of buoyancy (F_B). f) When the bubble pressure surpasses the interactions between the assembled NPs due to the continuous growth of the encapsulated bubble, the upper thin particulate shell is burst, creating a single hole in it to form the pot-like $MnFe_2O_4$ micromotor.

gradually diminish until the heating time (*t*) is prolonged to 10.5 s. At the same time, the image contrast between the oil and water phases increases, indicating the increase in the concentration of the $MnFe_2O_4$@OA NPs. Both of them are caused by the consecutive evaporation of the volatile oil, as evidenced by the successive formation-growth-disruption of the gas bubbles. At *t* between 18 and 38.2 s, the assembly of the $MnFe_2O_4$@OA NPs is observed to occur at the oil/water interface, leading to a dense particulate shell formed on the droplet surface with an encapsulated gas bubble. When *t* is further extended to 38.3 s or longer, the dense particulate shell is burst to create a single hole in it, revealing the formation of a pot-like hollow microparticle. This is assumed to originate from the increased pressure of the encapsulated gas bubble. It is clear that after experiencing the above three different stages, the tiny oil droplets containing $MnFe_2O_4$@OA NPs are transformed into pot-like $MnFe_2O_4$ hollow microparticles by the NP assembly.

Based on above observation, it can be seen that the step when the bubble capsule bursts through the particulate shell because of the high gas pressure of the encapsulated "growing bubble" plays a most vital role in the formation of the pot-like micromotors. It is the "growing-bubble"-templated self-assembly of hydrophobic NPs in a volatile oil droplet that is responsible for the formation of the pot-like micromotors, as described in Figure 2B. Figure 2B-a shows that the surfactant molecules (CTAB) would line up at the oil/water interface to reduce the surface tension of the oil droplet in the bulk water phase. The $MnFe_2O_4$@OA NPs in the oil droplet can be stably dispersed at first due to the steric repulsion between the OA chains of adjacent NPs.[12] Figure 2B-b,c shows that the oil phase would intensively evaporate via a successive formation-growth-disruption of the gas bubbles due to its low boiling point of about 60 °C,[13] as evidenced by the first stage of the structural transformation shown in Figure 2A (0–10.5 s). In this step, chloroform is dissolved out of the oil droplet through the oil–water interface into bulk water phase, producing an outward diffusion flow of chloroform and carrying $MnFe_2O_4$@OA NPs in the oil droplet to the oil–water interface, where the hydrophobic oleic chains covered on the surface of the $MnFe_2O_4$@OA NPs compress and attract each other to expel water and oil phase into the bulk to minimize the free energy of the system. As a result, the aggregation and self-assembly of adjacent NPs occur within the oil–water interface through the attractive hydrophobic interaction (Figure 2B-b).[12a,14] However, the concentration of the $MnFe_2O_4$@OA NPs within the oil–water interface is too low at this stage for the assembled $MnFe_2O_4$@OA NPs to form a dense particulate shell. Therefore, the continuously growing oil gas bubbles can penetrate the interface, and then disrupt when they contact with bulk water phase due to the sudden change of the surface tension and the water solubility of chloroform (Figure 2B-c). When most of solvents inside the oil droplet are evaporated, the size of the oil droplet is largely reduced, leading to the concentration of the NPs inside. Hence, more and more $MnFe_2O_4$@OA NPs are self-assembled at the oil–water interface due to the strong attractive hydrophobic interaction between those NPs, and a dense particulate shell is formed. In this case, the evaporated oil gas bubbles start to be trapped inside the oil droplet (Figure 2B-d). They grow slowly

and merge into a big bubble at the interior, forming a bubble capsule (Figure 2B-e), corresponding to the second stage of the structural transformation of the oil droplet shown in Figure 2A (18–38.2 s). In this bubble capsule, the oil phase is located between the outer assembled $MnFe_2O_4$ particulate shell and the encapsulated gas bubble. With t prolonging, the encapsulated gas bubble grows at the expense of the oil phase, further concentrating the $MnFe_2O_4$ NPs dispersed in the oil phase and leading to the continuous self-assembly of the $MnFe_2O_4$ NPs. With the ongoing evaporation of the oil solvents, the gas pressure of the encapsulated gas bubble increases because of the volume confined by the outer rigid $MnFe_2O_4$ particulate shell. Note that the encapsulated bubble would be biased toward the upper side of the oil droplet under the action of buoyancy (F_B) in the above process. This makes the upper particulate shell of the bubble capsule much thinner than the bottom one. When the gas pressure surpasses the interactions between the ensembled NPs, the upper thin particulate shell is burst, generating a single hole on the surface of the bubble capsule (Figure 2B–f), corresponding to the third stage of the structural transformation of the oil droplet shown in Figure 2A (38.3–50 s). The pot-like $MnFe_2O_4$ micromotors are finally produced at the complete evaporation of the oil solvents. Figure 2B also implies that the NP concentration (C_{NP}) in the oil droplet affects the bursting behaviors of the particulate shell and thus the size of the open hole due to the changes of the shell thickness and toughness with the C_{NP}. This assumption is verified by the data in Figure 1A and Figure S2 (Supporting Information), which indicate that when C_{NP} increases from 20, 40, to 60 mg mL^{-1}, the size of the open hole in the assembled pot-like $MnFe_2O_4$ microparticles decreases from 15, 10, to 8 μm. At C_{NP} of 20 mg mL^{-1}, the obtained particulate shell is too thin to maintain the spherical morphology of the $MnFe_2O_4$ microparticle so that they only show a distorted pot-like morphology.

According to the above formation mechanism, chloroform with a slight water solubility is essential for the formation of the bubble capsule and the subsequent pot-like structure. To determine this, we have conducted a control experiment, where the chloroform/*n*-hexane mixture oil is replaced with a pure *n*-hexane oil phase. In this condition, no outward flow occurs in the oil phase because of the immiscibility between *n*-hexane and water so that the concentration of the NPs on the surface of the oil droplet is too low to form a dense particulate shell. As a result, the oil droplet collapses into an irregular microparticle with the evaporation of *n*-hexane, as shown in Figure S3 (Supporting Information). On the other hand, the pot-like structures do not also form when the pure chloroform is used as the oil phase (Figure S4, Supporting Information). In comparison of these two contrast experiments shown in Figures S3 and S4 (Supporting Information), the outward diffusion flow and inward condensation of the $MnFe_2O_4$@OA NPs in the evaporating chloroform and *n*-hexane droplet, which brings about the self-assembly and concentration of the $MnFe_2O_4$@OA NPs, are clearly observed respectively. This indicates that in the chloroform/*n*-hexane mixture oil droplet (Figure 2), *n*-hexane plays an important role to stabilize the spherical oil droplet for keeping $MnFe_2O_4$@OA NPs inside, while chloroform is essential for driving inner $MnFe_2O_4$@OA NPs to the surface of the oil droplet due to their different solubility in the bulk water

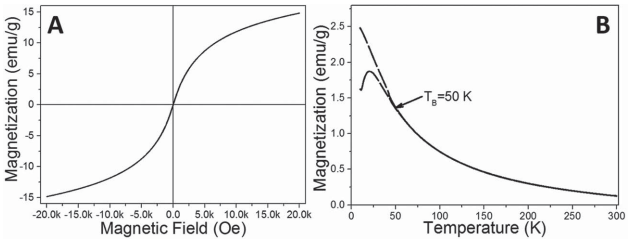

Figure 3. A) The magnetic hysteresis loop and B) ZFC–FC curves of the pot-like $MnFe_2O_4$ micromotors.

phase. As a result, the $MnFe_2O_4$@OA NPs tend to assemble at the oil–water interface to form a dense particulate shell, which is then burst through by the encapsulated growing gas bubble, resulting in an asymmetric pot-like structure. This concludes that we have developed a simple growing-bubble-templated NP assembly approach to fabricate pot-like $MnFe_2O_4$ hollow microparticles in a large scale. It is worthy of noting that as a simple approach to manufacture functional complex nanostructures, the NP assembly method has widely employed to fabricate ensembled particulate films, superlattices, chains, clusters, capsules, and hollow structures, etc.,[12b,15] but never used to obtain the asymmetric pot-like structure before. In fact, the growing-bubble-templated NP assembly approach developed in this work is a versatile method, and it could be extended to fabricate other metal oxide pot-like structures used for microreactors, energy storage, and conversion, as well as environment remediation.[10] As a demonstration, Figure S5 (Supporting Information) manifests that pot-like TiO_2 hollow microparticles are obtained when the $MnFe_2O_4$@OA NPs are replaced by TiO_2@OA NPs.

The as-fabricated pot-like $MnFe_2O_4$ micromotors have good magnetic properties, which are highly desired for the magnetically modulated motion. **Figure 3**A indicates that the as-obtained pot-like $MnFe_2O_4$ micromotors have a saturation magnetization (M_s) of 14.8 emu g^{-1}, as well as a negligible coercive force (H_c) and remanent magnetization (M_r) at 300 K, suggesting a superparamagnetic behavior. M_s of the pot-like $MnFe_2O_4$ micromotors is lower than that of bulk $MnFe_2O_4$ (80 emu g^{-1}).[16] This is possibly due to the spin canting and surface spin disorder,[17] which occurred in the nanosubunits ($MnFe_2O_4$ NPs, 6 nm) of the micromotor, as well as the high mass content of oleic acid (13.9 wt%, Figure 1E). To further probe the superparamagnetic behavior of the particles at room temperature, we have measured the field cooling (FC) and zero field cooling (ZFC) curves under a weak external field of 100 Oe. Figure 3B shows that with increasing temperature, the two curves begin to overlap at about 50 K, indicating a blocking temperature (T_B) of around 50 K, above which they are superparamagnetic, representing that the thermal energy of the particles is greater than the magnetic anisotropy energy or the energy barrier for the spin reorientation.[17] The superparamagnetic property of the as-fabricated pot-like $MnFe_2O_4$ micromotors could be explained by the fact that they are composed of self-assembled nanosubunits of $MnFe_2O_4$ NPs with a small size of about 6 nm. The superparamagnetic property cannot induce unfavorable aggregation of the $MnFe_2O_4$ micromotors, beneficial for the various applications.

Owing to the intensive catalytic decomposition of H_2O_2 over $MnFe_2O_4$,[18] the as-obtained $MnFe_2O_4$ pot-like micromotors can

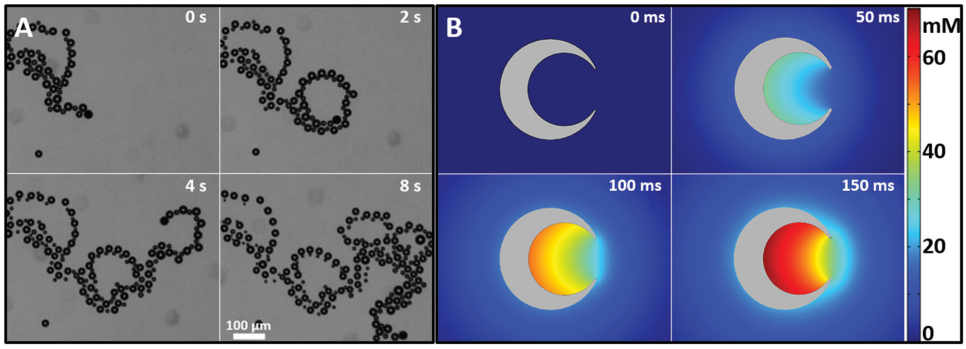

Figure 4. A) Time-lapse images of the autonomous motion of the $MnFe_2O_4$ micromotor in the fuel solution with 2 wt% H_2O_2 and 0.1 wt% CTAB (Video 2, Supporting Information) at different time intervals. B) The concentration of O_2 molecules distributed inside and outside the pot-like $MnFe_2O_4$ micromotor (in gray color) at different catalytic reaction times of 0, 50, 100, and 150 ms, indicating that the catalytically generated O_2 molecules are highly concentrated in the hollow interior of the motor, which would facilitate the nucleation and growth of O_2 into bubbles preferentially on the inner concave surface rather than on the outer convex surface, resulting in continuous ejection of O_2 bubbles from the open hole to propel the micromotor.

be self-propelled in the liquid media containing H_2O_2. Video 2 (Supporting Information) and **Figure 4**A show the autonomous motion of the pot-like $MnFe_2O_4$ micromotors in a 2 wt% H_2O_2 aqueous solution with 0.1 wt% CTAB. A long tail of O_2 bubbles with radius (r) of ≈7.5 μm is ejected from one side of the pot-like $MnFe_2O_4$ micromotor at a frequency (f) of about 30 Hz. This engenders a strong momentum that propels the micromotor forward with a remarkable speed of 260 μm s^{-1} (Figure 4A). Magnified microscopic images in Figure S6 (Supporting Information) reveal that the O_2 bubbles are formed inside the pot-like $MnFe_2O_4$ micromotor and then ejected from the open hole. A curved tail of O_2 bubbles in Figure 4A indicates that the motion of the micromotor follows a spiral ballistic trajectory, suggesting that the bubble releasing direction deviates from the symmetry axis of the pot-like $MnFe_2O_4$ micromotors, which generates a rotational torque besides the translational propulsion.[3b] The micromotor is observed to have a long life time due to the high stability of both $MnFe_2O_4$ and the catalytic H_2O_2 reaction over its surface.

Most of the previously reported bubble-propelled catalytic micromotors have complex structures and require tedious and expensive fabrication technologies, such as the "rolled-up," vapor deposition, and template-assisted electrodeposition methods.[7,19] They are composed of at least two components with an asymmetric Janus structure or multilayered tubular structure in which one is a catalytic reactive component and the other is an inert substance.[2a,f] In contrast, the as-obtained $MnFe_2O_4$ micromotors have a remarkable advantage of a simple single-layered structure and could be fabricated by a facile, versatile, and large-scale growing-bubble-templated NP assembly fabrication approach. To get the single-layered micromotor moving, an asymmetric structure is necessary to generate an asymmetric distribution of chemical species and subsequently break the symmetry of the pressure distribution, eventually resulting in the directional motion of the motor.[6g] The pot-like structure, as a typical asymmetric structure, has different concave and convex shapes in the inner and outer surfaces, respectively. Thus, it may lead to an asymmetric bubble formation. For example, Huang and co-workers[20] have reported that for the Pt/Ag/Au multilayered nanoshell micromotor, the nucleation of bubbles on a concave surface is much easier than that on a convex surface according to the heterogeneous nucleation energy. However, in the calculation it is assumed that the supersaturation of solutes is at a same level near the concave and convex surfaces of the micromotor.

Here, we propose that the asymmetric concentration distribution of the solutes on the concave and convex surfaces before bubble nucleation plays a much important role in the preferable bubble nucleation and growth on the concave surface since a certain level of solute supersaturation is a prerequisite condition for the bubble nucleation. To confirm this, we follow Fick's second law of diffusion[21] and construct a 2-dimensional model by the transient diffusion module of COMSOL multiphysics. Figure 4B illustrates that the O_2 concentration distribution in the interior space confined by the concave surface and the outer space away from the convex surface have completely different dependences on the diffusion time. When O_2 molecules are generated at a rate (K) of 3.1 mmol m^{-2} s^{-1} on both the concave and convex surfaces of the pot-like $MnFe_2O_4$ micromotor (the case of Figure 4A), the ratio of the O_2 concentration on the concave surface (C_c) to that on the convex surface (C_v) ($R = C_c/C_v$), which represents the asymmetry of O_2 concentration distribution between them, reaches a maximum value of 3.6 with a diffusion time of 0.15 s. The O_2 molecules in the confined space of the micromotor will reach the maximum supersaturation concentration for the O_2 bubble nucleation (68×10^{-3} M[22]) within 0.15 s due to the accumulative effect of the inner confined void, while those generated on the outer convex surface continuously diffuse away from the surface and cannot effectively accumulate to form bubbles. This result indicates that O_2 can easily nucleate and grow into bubbles in the confined void because of the high concentration of the catalytically generated O_2 molecules, which are then ejected from the open hole to propel the micromotor, as the propulsion mechanism shown in Figure 6A.

According to above analysis, the outer convex surface of the micromotor is also reactive for the catalytic decomposition of H_2O_2 even though no obvious O_2 bubble is observed on it. Instead, the O_2 molecules generated catalytically on the convex surface will quickly diffuse away. In order to confirm this, we have carefully observed the size change of an O_2 bubble attached on the convex surface of a moving micromotor, as shown in Figure S7 (Supporting Information). As expected, the size of

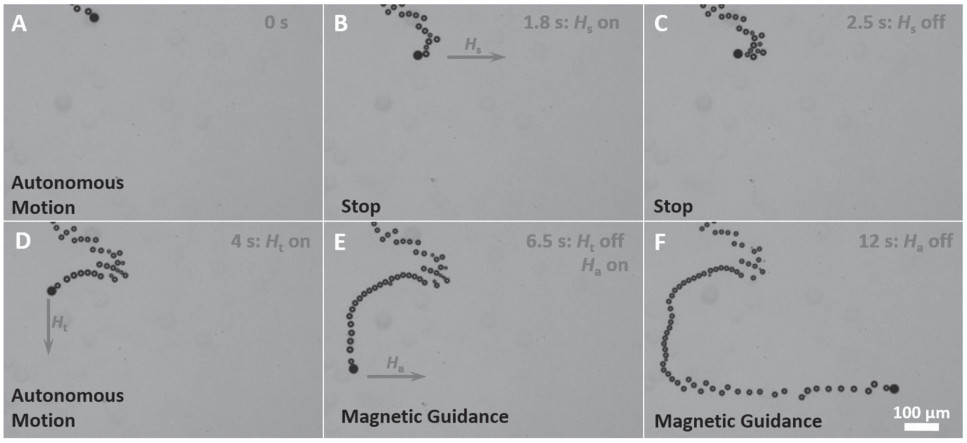

Figure 5. Time-lapse images of the A,D) autonomous motion, B,C) magnetically controlled stop, and E,F) magnetic guidance of the $MnFe_2O_4$ micromotor in the fuel solution with 2 wt% H_2O_2 and 0.1 wt% CTAB (Video 3, Supporting Information) at time intervals of A) 0, B) 1.8, C) 2.5, D) 4, E) 6.5, and F) 12 s.

this bubble continuously increases as long as it still attaches to the convex surface of the moving micromotor, indicating the continuous generation of O_2 on the convex surface. For the pot-like micromotors with the open hole in different sizes produce different confining effects, R will also vary. Figure S8 (Supporting Information) shows that R at a diffusion time of 0.1 s increases from 2.5, 3.3, to 3.6 when the open hole of the micromotor decreases from 18, 10, to 4 µm, respectively. This indicates that for the pot-like micromotor, the smaller the size of the open hole is, the higher the concentration asymmetry of the catalytic resultants within and out of the micromotor is, which facilitates the nucleation and growth of O_2 bubbles selectively on the inner concave surface. However, it is also imaginable that the small open hole (<10 µm in size) may affect the continuous feeding of the fuel as it could be easily blocked by the formed bubbles (10–20 µm in size, Figure 4A), inhabiting the continuous ejection of bubbles and the self-propulsion of the pot-like micromotor. When the open hole of the pot-like micromotor is too large (close to the diameter of the micromotor), the concentration asymmetry of the catalytic resultants within and out of the micromotor may be too low to trigger the preferable bubble nucleation on the concave surface. For example, the single-component "coconut" Pt micromotor reported very recently shows that the O_2 bubbles are generated on the convex surface,[23] which may be caused by the contamination of inner concave surface in the preparation process, as well as the low asymmetry of O_2 concentration because of the large open hole.

Attributing to the promising magnetic property (M_s = 14.8 emu g^{-1} = 14.8 A m^2 kg^{-1}), the as-obtained pot-like $MnFe_2O_4$ micromotor have a good response to the external magnetic field, and their motion of the micromotor could be modulated magnetically, as shown in Video 3 (Supporting Information) and **Figure 5**. Figure 5A–C shows that the moving micromotor could be stopped when a magnet with a surface magnetic flux density of 0.33 Tesla (T), which produces a gradient magnetic field (H_s) with values depending on its distance from the micromotor, is close to it at a distance of about 17 mm along the direction opposite to its motion direction. After the magnetic field is withdrawn, the autonomous motion of the micromotor recovers (Figure 5D), representing the magnetically "stop-and-go" operations of the micromotor. Figure S9 (Supporting Information) shows the magnetic flux density (B) versus the distance (x) between the micromotor and magnet, indicating that it decreases exponentially with x according to Equation (1) in which B_0, a, and t are constants with the value of 0.3173, 157.2, and 0.0127, respectively.

$$B_x = B_0 e^{-ax} + t \tag{1}$$

In a gradient magnetic field H_s, the magnetic micromotor is subjected to a magnetic force as follows

$$F_{mag} = \mu_0 M_M \cdot \nabla H \tag{2}$$

Here, H is the magnetic field intensity in T, μ_0 is the magnetic susceptibility of the free space ($4\pi \times 10^{-7}$ H m^{-1}), and M_M is the magnetization of the micromotor. Since we are interested in the magnetic force opposite to the motion direction of the micromotor (x-direction) only, the magnetic force on it finally reduces to

$$F_{mag} = \mu_0 M_V V \frac{dH_x}{dx} = M_V V \frac{dB_x}{dx} \tag{3}$$

Here, M_v represents the volume magnetization of the micromotor (3.65×10^3 A m^{-1}), which is calculated from the M–H curve in Figure 3. V is the volume of the micromotor (5.13×10^{-15} m^3). dB_x/dx represents the gradient of magnetic flux density at x-direction. The force analysis of the micromotor under the applied magnetic force is shown in Figure S10 (Supporting Information).

The magnetic force exerted (x = 17 mm) to stop the micromotor (Figure S10A, Supporting Information) can be calculated from Equation (3) to be 6.5×10^{-11} N. This force is close to the driving force of the autonomous micromotor ($F_d = 5.8 \times 10^{-11}$ N), which is calculated as follows

$$F_d = 6\pi r \eta v \tag{4}$$

Here, r and v are 12.5 µm and 200 µm s^{-1}, referring the radius and speed of the autonomous moving micromotor in

Figure 5. η is the dynamic viscosity of the aqueous medium (1.23×10^{-3} Pa s).[24] The magnetic force on the magnetic micromotor can be considered as the sum of the individual forces on each single-domain or single superparamagnetic $MnFe_2O_4$ NP. Due to the asymmetric distribution of the $MnFe_2O_4$ NPs in the pot-like $MnFe_2O_4$ micromotor (Figure 1B), the exerted magnetic force near the open hole is far weaker than that away from it due to the small number of the $MnFe_2O_4$ NPs. As a result, the acting point (O_M) of the magnetic force (F_{mag}) is separated from the geometric center (O_G) of the micromotor with a distance of l, as shown in Figure S10B (Supporting Information). If a gradient magnetic field is applied at the direction perpendicular to that of the motion of the micromotor, a torque ($M_o = F_{mag} \times l$) is generated to turn the autonomous micromotor until its moving direction is along with that of the magnetic force (Figure S10B, Supporting Information). As shown in Figure 5E, the autonomous micromotor is turned with a negligible speed variation to the direction of the applied gradient magnetic field (H_t) with an F_{mag} of 1.26×10^{-11} N. In addition, the micromotor can be accelerated from 200 to 390 μm s^{-1} by applying a gradient magnetic field (H_a) at the same direction of the motion of the micromotor (Figure 5F), which exerts a magnetic force of 1.17×10^{-10} N on the micromotor (Figure S10C, Supporting Information). Such on-demand control of the movement of the $MnFe_2O_4$ micromotor promises their diverse applications such as cargo transportation and environmental remediation, etc. Compared to the previously reported magnetic controllable catalytic micromotors with complex multilayered structures,[5,25] the as-developed $MnFe_2O_4$ micromotor achieves the self-propulsion as well as the magnetic controllable motion with a simple single-layered structure due to the combination of the catalytic activity and the excellent magnetic response of the $MnFe_2O_4$. Moreover, its motion is guided by a gradient magnetic field, which can be applied by an electromagnet or permanent magnet, and has a promising advantage of easy operation. This is of importance for the large-scale environmental applications (e.g., water treatment) of the micromotors. In contrast, for the previous micro-/nanomotors to keep a constant speed,[5,19] the magnetic control is generally realized by a uniform magnetic field, which requires complex 3D Helmholtz coils to generate, and is difficult to apply in a long distance. Additionally, for such catalytic bubble-propelled micromotors with simple structures as irregular shaped MnO_2 and "coconut" Pt micromotors,[3g,23] it is difficult to control the motion as they hardly respond to the external stimuli at room temperature.

The removal of spilt oil from contaminated water is of considerable importance for minimizing environmental hazards. Wang and co-workers[9] have very recently demonstrated the separation of oil droplets from water by the dodecanethiol-modified multilayered Au/Ni/poly(3,4-ethylenedioxythiophene)/Pt tubular microengines and Mg/Ti/Ni/Au Janus micromotors, indicating a promising platform for the effective oil–water separation by self-propelled micromotors. However, these micromotors suffer from disadvantages of complex structures, sophisticated fabrication process, and high cost, which greatly hinder their widespread use. In comparison, the as-developed $MnFe_2O_4$ micromotors have a simple structure, which can be easily obtained by a facile NP self-assembly method. Moreover, they can be directly used for the environmental oil remediation without any further surface modification because of the hydrophobility of the pre-existed long oleic acid chains on the surface. As demonstrated in **Figure 6**A, the $MnFe_2O_4$ micromotor with pre-existed long oleic acid chains could perform "on-the-fly" collection of oil droplets through hydrophobic surface–oil interaction. Video 4 (Supporting Information) and Figure 6B demonstrate that with the guidance of an external magnetic field and its autonomous motion, the $MnFe_2O_4$ micromotor can approach (Figure 6B-a–c), capture (Figure 6B-d,e), and transport (Figure 6B-f) the oil droplets (1-octane) in the liquid medium containing 2 wt% H_2O_2 and 0.5 wt% Triton-X100. Once the micromotor contacts an oil droplet (about 20 μm in size), it instantaneously captures the oil droplet. Hence, for the potential practical application of the $MnFe_2O_4$ micromotors in the oil removal, the micromotors could capture oil droplets in a wide area by using their self-propulsion and collect them through magnetic separation. In addition, the micromotors in the treated area could be magnetically guided to the untreated areas for further capturing oil droplets. Video 4 (Supporting Information) indicate that the micromotor can carry up to three oil droplets, reflecting the large drag force. The micromotor moves initially at a speed of 112 μm s^{-1}. As expected, the speed of the micromotor decreases linearly from 86 to 23 μm s^{-1} with increasing the number of the carried oil droplets from 1 to 3, as shown in Figure S11 (Supporting Information). Figure S12 (Supporting Information) shows that no oil droplet can be captured by the micromotor when the ionic surfactant of CTAB is used in the liquid medium. It can be ascribed to the CTAB adsorbed on the micromotor surface, resulting in the electrostatic repulsion between the positively charged surface of the oil droplet and the micromotor. This implies that the type of the surfactant in the liquid medium also plays an important role in the affinity of the hydrophobic micromotor with the oil droplet. The above results indicate that the as-fabricated $MnFe_2O_4$ micromotors have a promising potential for facile, rapid, and highly efficient collection of oil in the oil-contaminated water.

3. Conclusion

In this work, we have developed a novel magnetically modulated self-propelled micromotor using simple pot-like hollow microparticles assembled with $MnFe_2O_4$ NPs. The as-designed micromotors can be easily fabricated in a large scale by a growing-bubble-templated NP assembly approach. In this approach, the hydrophobic $MnFe_2O_4$@OA NPs in the volatile oil droplet of chloroform and *n*-hexane are driven to its surface (oil/water interface) due to the outward diffusion of chloroform and assembled into a dense particulate shell under the surface hydrophobic interactions of $MnFe_2O_4$@OA NPs. This dense $MnFe_2O_4$ particulate shell is then burst due to the growing dimension and increased internal pressure of the encapsulated gas bubble generated by the continuously vaporized oil phase, subsequently creating a single hole in the shell and resulting in the asymmetric pot-like $MnFe_2O_4$ micromotors. The as-obtained simple pot-like $MnFe_2O_4$ micromotors can efficiently integrate three interesting properties, including the high catalytic activity for H_2O_2 decomposition, superior magnetic property, as well as instinctive surface hydrophobicity. Hence, they

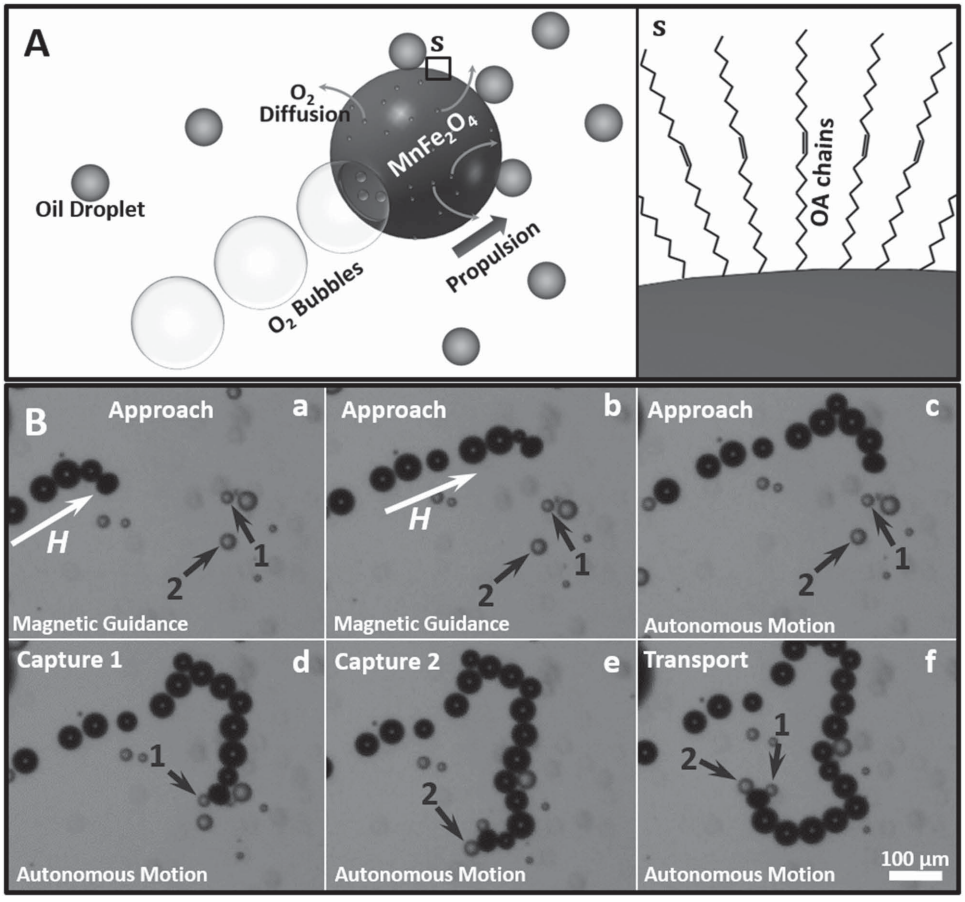

Figure 6. A) Schematic demonstration of the bubble propulsion and of the pot-like $MnFe_2O_4$ micromotor attributing to selective nucleation and growth of O_2 bubbles on its inner concave surface, as well as the removal of oil droplets by the micromotor due to their hydrophobic outer surfaces. B) Time-lapse images taken from Video 4 in the Supporting Information, indicating that an $MnFe_2O_4$ micromotor is approaching under the a,b) magnetic guidance and c) autonomous motion, d,e) capturing and f) transporting the oil droplets (1 and 2) at a) 0, b) 1, c) 2, d) 3.5, e) 5 and f) 7 s, respectively.

can show not only a bubble-propelled motion with strong thrust in an aqueous medium but also their motion direction and speed can both be wirelessly modulated by an external magnetic field. Furthermore, they can be directly used for environmental oil remediation without any further surface modification attributing to the long oleic acid chains pre-existant in the surfaces. The mechanism of the self-propulsion of the pot-like single-component $MnFe_2O_4$ micromotor has been proposed based on the fact that the catalytically generated O_2 molecules would nucleate and grow into bubbles preferentially on the inner concave surface rather than on the outer surface, resulting in continuous ejection of O_2 bubbles from the open hole to propel the micromotor. The micromotor developed here may inspire novel practical micromotors due to the low cost, simple structure, as well as the facile, large-scale fabrication strategy.

4. Experimental Section

Synthesis of $MnFe_2O_4$@OA NPs: $MnFe_2O_4$@OA NPs were synthesized by a modified solvothermal method.[26] At first, 3.39 g oleic acid, 2 mmol of ferric nitrate, and 1 mmol of manganous acetate were dissolved in 10 mL ethanol. Then 2 mL of 5×10^{-3} M NaOH aqueous solution was added into the above solution. After that, the prepared solution was transported to a 100 mL autoclave. The autoclave was sealed and placed in an oven at 180 °C for 16 h, and then naturally cooled down at room temperature. The obtained NPs were washed by the mixture solution containing *n*-hexane and ethanol four times, volume ratio of which is 1:3, and subsequently isolated by centrifugation at 8000 rpm for 2 min. Finally, the collected NPs were dried in an oven at 60 °C for 8 h.

Preparation of $MnFe_2O_4$ Micromotors: The pot-like $MnFe_2O_4$ micromotors are fabricated by a growing-bubble-templated assembly of hydrophobic $MnFe_2O_4$@OA NPs in a suspension of volatile oil droplets suspended in an aqueous solution (Figure 3B). At first, an oil phase was prepared by dispersing the $MnFe_2O_4$ NPs (40 mg mL^{-1}) in a mixture solvent containing chloroform and *n*-hexane (8.8:1.2 in volume). Then, 0.2 mL of the oil phase were added into 300 mL water containing 3.0×10^{-3} M CTAB (water phase) with magnetic stirring for 60 s to obtain an aqueous suspension of oil emulsion droplets. Then, the resulted suspension was heated at 37 °C for 160 s with a water bath, and then stood under static conditions at room temperature for 90 min. Finally, the resulting brown precipitates were isolated by magnetic separation, washed once with water at 60 °C, and then dried in vacuum to obtain the pot-like $MnFe_2O_4$ micromotors.

Pot-like TiO_2 hollow microparticles were also prepared by the growing-bubble-templated assembly of hydrophobic TiO_2@OA NPs, which were prepared by a modified solvothermal method[27] with a titanium butoxide/OA ratio of 1:5.

Sample Characterization: Scanning electron microscopy (SEM) was obtained using a Hitachi S-4800 Field-emission SEM (Japan). The XRD patterns of the samples were recorded using a Rigaku D/Max-2000

diffractometer equipped with a Cu K radiation source ($\lambda = 0.15418$ nm). TG–DSC analysis was carried out on a NETZSEC STA-449C thermal analyzer (Germany). The magnetic properties of the samples were investigated using a physical property measurement system (Model PPMS-9, Quantum Design, USA).

Preparation of the Fuel Solutions: The 2 wt% H_2O_2 aqueous solutions containing 0.1 wt% CTAB or 0.5 wt% Triton-X100 were freshly prepared before the microscopy observation.

Recording Microscopy Videos and Analysis: 10 µL aqueous suspension containing $MnFe_2O_4$ micromotors was added into 320 µL of the fuel solution with 2 wt% H_2O_2 and 0.1 wt% CTAB. The motion of $MnFe_2O_4$ micromotors were observed and recorded at room temperature through an optical microscope (Leica DMI 3000M). The 1-octane oil droplets were prepared by dispersing 1-octane in water (1:100 in volume) with 0.5 wt% Triton-X100. The approaching, capturing, and transporting of the 1-octane oil droplets by the micromotors in the fuel solution with 2 wt% H_2O_2 and 0.5 wt% Triton-X100 were also recorded. All videos of the micromotors' movement were analyzed using Video Spot Tracker V08.01 software.

Supporting Information

Supporting Information is available from the Wiley Online Library or from the author.

Acknowledgements

F.Z.M. and D.P. contributed equally to this work. This work was supported by the National Natural Science Foundation of China (21474078, 51303144 and 51521001), the Top Talents Lead Cultivation Project and Natural Science Foundation of Hubei Province (2012FFB05101 and 2015CFA003), the Self-determined and Innovative Research Funds of SKLWUT and WUT (2013-PY-3), and the Fundamental Research Funds for the Central Universities (WUT: 2013-IV-089).

Received: July 10, 2015
Revised: August 13, 2015
Published online: September 9, 2015

[1] a) J. Wang, *Nanomachines: Fundamentals and Applications*, Wiley-VCH, Weinheim, Germany **2013**; b) W. Wang, W. Duan, S. Ahmed, T. E. Mallouk, A. Sen, *Nano Today* **2013**, *8*, 531.

[2] a) M. Guix, C. C. Mayorga-Martinez, A. Merkoçi, *Chem. Rev.* **2014**, *114*, 6285; b) D. Patra, S. Sengupta, W. Duan, H. Zhang, R. Pavlick, A. Sen, *Nanoscale* **2013**, *5*, 1273; c) S. Sengupta, M. E. Ibele, A. Sen, *Angew. Chem. Int. Ed.* **2012**, *51*, 8434; d) W. Gao, J. Wang, *ACS Nano* **2014**, *8*, 3170; e) S. Sanchez, L. Soler, J. Katuri, *Angew. Chem. Int. Ed.* **2015**, *54*, 1414; f) V. Magdanz, M. Guix, O. Schmidt, *Robot. Biomim.* **2014**, *1*, 1; g) Z. G. Wu, Y. J. Wu, W. P. He, X. K. Lin, J. M. Sun, Q. He, *Angew. Chem. Int. Ed.* **2013**, *52*, 7000; h) J. G. S. Moo, M. Pumera, *Chem. Eur. J.* **2015**, *21*, 58.

[3] a) F. Mou, C. Chen, H. Ma, Y. Yin, Q. Wu, J. Guan, *Angew. Chem. Int. Ed.* **2013**, *52*, 7208; b) F. Mou, C. Chen, Q. Zhong, Y. Yin, H. Ma, J. Guan, *ACS Appl. Mater. Interfaces* **2014**, *6*, 9897; c) Y. Mei, G. Huang, A. A. Solovev, E. B. Ureña, I. Mönch, F. Ding, T. Reindl, R. K. Y. Fu, P. K. Chu, O. G. Schmidt, *Adv. Mater.* **2008**, *20*, 4085; d) K. M. Manesh, M. Cardona, R. Yuan, M. Clark, D. Kagan, S. Balasubramanian, J. Wang, *ACS Nano* **2010**, *4*, 1799; e) A. A. Solovev, Y. F. Mei, E. B. Urena, G. S. Huang, O. G. Schmidt, *Small* **2009**, *5*, 1688; f) W. Gao, A. Uygun, J. Wang, *J. Am. Chem. Soc.* **2012**, *134*, 897; g) H. Wang, G. Zhao, M. Pumera, *J. Am. Chem. Soc.* **2014**, *136*, 2719.

[4] a) W. Gao, S. Sattayasamitsathit, J. Orozco, J. Wang, *J. Am. Chem. Soc.* **2011**, *133*, 11862; b) J. Wang, *Faraday Discuss.* **2013**, *164*, 9; c) M. Manjare, B. Yang, Y. P. Zhao, *Phys. Rev. Lett.* **2012**, *109*, 128305.

[5] J. Wang, K. M. Manesh, *Small* **2010**, *6*, 338.

[6] a) Z. Wu, X. Lin, Y. Wu, T. Si, J. Sun, Q. He, *ACS Nano* **2014**, *8*, 6097; b) Z. Liu, J. Li, J. Wang, G. Huang, R. Liu, Y. Mei, *Nanoscale* **2013**, *5*, 1345; c) S. Sanchez, A. N. Ananth, V. M. Fomin, M. Viehrig, O. G. Schmidt, *J. Am. Chem. Soc.* **2011**, *133*, 14860; d) T. L. Xu, F. Soto, W. Gao, V. Garcia-Gradilla, J. X. Li, X. J. Zhang, J. Wang, *J. Am. Chem. Soc.* **2014**, *136*, 8552; e) A. A. Solovev, E. J. Smith, C. C. B. Bufon, S. Sanchez, O. G. Schmidt, *Angew. Chem. Int. Ed.* **2011**, *50*, 10875; f) Z. Wu, X. Lin, X. Zou, J. Sun, Q. He, *ACS Appl. Mater. Interfaces* **2015**, *7*, 250; g) F. Mou, Y. Li, C. Chen, W. Li, Y. Yin, H. Ma, J. Guan, *Small* **2015**, *11*, 2564.

[7] Y. Mei, A. A. Solovev, S. Sanchez, O. G. Schmidt, *Chem. Soc. Rev.* **2011**, *40*, 2109.

[8] a) Y. F. Mei, A. A. Solovev, S. Sanchez, O. G. Schmidt, *Chem. Soc. Rev.* **2011**, *40*, 2109; b) W. Gao, S. Sattayasamitsathit, A. Uygun, A. Pei, A. Ponedal, J. Wang, *Nanoscale* **2012**, *4*, 2447.

[9] a) W. Gao, X. Feng, A. Pei, Y. Gu, J. Li, J. Wang, *Nanoscale* **2013**, *5*, 4696; b) M. Guix, J. Orozco, M. García, W. Gao, S. Sattayasamitsathit, A. Merkoçi, A. Escarpa, J. Wang, *ACS Nano* **2012**, *6*, 4445.

[10] a) S. H. Im, U. Y. Jeong, Y. N. Xia, *Nat. Mater.* **2005**, *4*, 671; b) W. Wang, M.-J. Zhang, R. Xie, X.-J. Ju, C. Yang, C.-L. Mou, D. A. Weitz, L.-Y. Chu, *Angew. Chem. Int. Ed.* **2013**, *125*, 8242; c) D. C. Hyun, P. Lu, S.-I. Choi, U. Jeong, Y. Xia, *Angew. Chem. Int. Ed.* **2013**, *52*, 10468.

[11] S. Sun, H. Zeng, D. B. Robinson, S. Raoux, P. M. Rice, S. X. Wang, G. Li, *J. Am. Chem. Soc.* **2004**, *126*, 273.

[12] a) A. Sánchez-Iglesias, M. Grzelczak, T. Altantzis, B. Goris, J. Pérez-Juste, S. Bals, G. Van Tendeloo, S. H. Donaldson, B. F. Chmelka, J. N. Israelachvili, L. M. Liz-Marzán, *ACS Nano* **2012**, *6*, 11059; b) Y. Lin, H. Skaff, T. Emrick, A. D. Dinsmore, T. P. Russell, *Science* **2003**, *299*, 226; c) A. K. Boal, F. Ilhan, J. E. DeRouchey, T. Thurn-Albrecht, T. P. Russell, V. M. Rotello, *Nature* **2000**, *404*, 746.

[13] L. H. Horsley, *Azeotropic Data-III*, Advances in Chemistry, Vol. 116, American Chemical Society, Washington, DC **1973**.

[14] P. Qiu, C. Jensen, N. Charity, R. Towner, C. Mao, *J. Am. Chem. Soc.* **2010**, *132*, 17724.

[15] a) Z. Nie, A. Petukhova, E. Kumacheva, *Nat. Nanotechnol.* **2010**, *5*, 15; b) M. Grzelczak, J. Vermant, E. M. Furst, L. M. Liz-Marzán, *ACS Nano* **2010**, *4*, 3591; c) L. Hu, M. Chen, X. Fang, L. Wu, *Chem. Soc. Rev.* **2012**, *41*, 1350; d) J.-W. Liu, H.-W. Liang, S.-H. Yu, *Chem. Rev.* **2012**, *112*, 4770; e) L. Xu, W. Ma, L. Wang, C. Xu, H. Kuang, N. A. Kotov, *Chem. Soc. Rev.* **2013**, *42*, 3114; f) Y. Min, M. Akbulut, K. Kristiansen, Y. Golan, J. Israelachvili, *Nat. Mater.* **2008**, *7*, 527; g) W. Luo, H. Ma, F. Mou, M. Zhu, J. Yan, J. Guan, *Adv. Mater.* **2014**, *26*, 1058; h) M. S. Wong, J. N. Cha, K.-S. Choi, T. J. Deming, G. D. Stucky, *Nano Lett.* **2002**, *2*, 583.

[16] E. P. Wohlfarth, K. H. J. Buschow, *Handbook of Magnetic Materials*, North-Holland, Amsterdam **2001**.

[17] U. Jeong, X. W. Teng, Y. Wang, H. Yang, Y. N. Xia, *Adv. Mater.* **2007**, *19*, 33.

[18] a) P. Lahiri, S. K. Sengupta, *Can. J. Chem.* **1991**, *69*, 33; b) T. Valdés-Solís, P. Valle-Vigón, S. Álvarez, G. Marbán, A. B. Fuertes, *Catal. Commun.* **2007**, *8*, 2037.

[19] H. Wang, M. Pumera, *Chem. Rev.* **2015**, *115*, 8704.

[20] W. Huang, M. Manjare, Y. Zhao, *J. Phys. Chem. C* **2013**, *117*, 21590.

[21] P. Han, D. M. Bartels, *J. Phys. Chem.* **1996**, *100*, 5597.

[22] M. B. Rubin, R. M. Noyes, *J. Phys. Chem.* **1987**, *91*, 4193.

[23] G. Zhao, M. Pumera, *Nanoscale* **2014**, *6*, 11177.

[24] K. Manna, A. Panda, *J. Surfactants Deterg.* **2011**, *14*, 563.

[25] G. Huang, J. Wang, Y. Mei, *J. Mater. Chem.* **2012**, *22*, 6519.

[26] S. Jovanović, M. Spreitzer, M. Tramšek, Z. Trontelj, D. Suvorov, *J. Phys. Chem. C* **2014**, *118*, 13844.

[27] C.-T. Dinh, T.-D. Nguyen, F. Kleitz, T.-O. Do, *ACS Nano* **2009**, *3*, 3737.